nature catalysis

Article

https://doi.org/10.1038/s41929-023-00996-3

The role of surface hydroxyls in the entropy-driven adsorption and spillover of H_2 on Au/TiO_2 catalysts

In the format provided by the authors and unedited

Supplementary Materials

The PDF file includes:

Supplementary Methods
Supplementary Discussion
Supplementary Figs. 1 to 19
Supplementary Tables 1 to 6
Supplementary References

Contents

Supplementary Methods

Au particle size and site analysis

The fraction of Au on the surface (%S) and perimeter (%P) was determined using methods adapted from the literature, modeling the Au particles as cubooctahedra.[1] The number of Au atoms in a particle (of volume, V_{Au}), on the surface (the surface area, S_{Au}) and along the perimeter (P_{Au}, i.e. at the metal-support interface) was determined using Supplementary Equations 1, 2 and 3, respectively. A cuboctahedron has 12 vertices or corners (C_{Au}) so, the number of corner atoms is constant (12) regardless of particle size; the fraction of corner sites simply changes with the particle volume. (A helpful tool for these conversions is available at: https://rechneronline.de/pi/cuboctahedron.php).

$$V_{Au} = \frac{5D_p^3\rho_{Au}\sqrt{2}}{24m_{Au}} \quad (1)$$

$$S_{Au} = \frac{D_p^2(3+\sqrt{3})}{2\pi r_{Au}^2} \quad (2)$$

$$P_{Au} = \frac{D_p}{r_{Au}} \quad (3)$$

$$C_{Au} = 12 \quad (4)$$

Where:

- V_{Au} is the total number of Au atoms in a particle of given diameter
- D_p is the circumsphere diameter of a cuboctahedral particle (measured from TEM)
- ρ_{Au} is the bulk density of Au (19300 kg/m^3)
- m_{Au} is the mass of a single Au atom (3.27×10^{-25} kg/atom)
- S_{Au} is the total number of Au atoms on the surface of one particle of a given diameter
- r_{Au} is the atomic radius of Au (1.66×10^{-10} m/atom)
- P_{Au} is the total number of Au atoms on the perimeter of the base in one particle of a given diameter
- C_{Au} is the total number of Au atoms at the corners in one particle of a given diameter

The fraction of the Au atoms on the surface, perimeter at the corner of any given particle can be determined by dividing Supplementary Equation 2, 3 or 4 by Supplementary Equation 1, respectively, as shown in Supplementary Equations 5 – 7.

$$\%S = \frac{12m_{Au}(3+\sqrt{3})}{5\pi D_p r_{Au}^2 \rho_{Au}\sqrt{2}} \quad (5)$$

$$\%P = \frac{24m_{Au}}{5D_p^2 r_{Au}\rho_{Au}\sqrt{2}} \quad (6)$$

$$\%C = \frac{288m_{Au}}{5D_p^3\rho_{Au}\sqrt{2}} \quad (7)$$

$$Au_{sur}\left(\frac{\mu mol}{g\ cat.}\right) = \frac{\%Au \times \%Sur \times 10^6}{M_w(Au)} \quad (8)$$

$$Au_{per}\left(\frac{\mu mol}{g\ cat.}\right) = \frac{\%Au \times \%Per \times 10^6}{M_w(Au)} \quad (9)$$

where:

- %S is the Au surface fraction expressed as a percent
- %P is the Au perimeter fraction expressed as a percent
- %C is the Au corner fraction expressed as a percent

Using the average particle diameter to determine fractions of surface and perimeter atoms leads to unnecessary errors in these values. The core problem is that the fraction of surface and perimeter atoms per particle has a greater dependence on the particle diameter than does the arithmetic mean diameter. Thus, the heterogeneity intrinsic in particle size distributions skews perimeter and surface atom fractions determined using only the average particle diameter. This problem becomes more acute as particle size distributions become wider.

To account for the heterogeneity in the particle size distribution, %S, %P, and %C were determined for each bin in the particle size histogram. At least 200 nanoparticles were considered, using bin sizes of 0.2 nm. For a particle diameter in the center of each bin, S_{Au}, P_{Au}, and C_{Au} were determined using Supplementary Equations 2, 3, and 4, respectively. These values were then multiplied by the histogram frequency of that bin to account for the particle size distribution. The individual solutions to these equations were summed across all bins estimate the total fraction of each type of site for each catalyst. These numbers were then used to determine the %S, %P, and %C using Supplementary Equations 5, 6, and 7, respectively.

Computational Methods

Plane wave based density functional theory (DFT) calculations with periodic boundary conditions were performed using the Vienna Ab Initio Simulation Package (VASP).[2-4] Exchange and correlation were described with the BEEF-vdW functional[5] and the projector augmented wave (PAW) method was used to approximate the core electronic structure.[6,7] A plane wave energy cutoff of 400 eV was used for all the calculations.

For the slab models Gaussian smearing was employed with a Fermi temperature of $k_bT = 0.01$ eV and the total energy was extrapolated to $k_bT = 0.0$ eV. Residual forces on equilibrium geometries were converged to below 0.01 eV/Å. For TiO_2 slab models. Monkhorst-Pack k-point meshes of $(1 \times 1 \times 1)$ and $(4 \times 4 \times 1)$ were used for models based on (10×5) and (2×1) unit cells respectively to sample the Brillouin zone. Dipole correction was applied to electrostatic potential in the *z* direction for all the slab models.

Proton adsorption was calculated on a (10×5) sized $TiO_2(110)$ surface unit cell as shown in **Supplementary Figure 2** (a and b), corresponding to a surface coverage of 0.1 H^+/e^- per nm^2. For a higher coverage of 2.5 H^+/e^- per nm^2, we employed a smaller (2×1) surface unit cell as shown in **Supplementary Figure 2** (c and d). Both sides of the TiO_2 surfaces are fully hydroxylated by dissociating water molecules resulting in pairs of bridge-hydroxyl groups (HO_{br}) and coordinatively unsaturated (cus) hydroxyl groups (HO_{cus}). The thickness of the smaller (2×1) unit

cell was set to six layers, whereas the thickness for the larger (10 × 5) unit cell was reduced to 4 layers of titanium ions. Reduction of the thickness of the large hydroxylated slab model was necessary because it contains 400 titanium atoms, 900 oxygen atoms and 200 hydrogen atoms before proton adsorption and approaches the limits of computational feasibility.

The proton was adsorbed on the cus-hydroxyl site forming a water molecule. The cus-hydroxyls were previously[8,9] found to be the most stable sites for the H species formed upon dissociative H_2 adsorption. All atoms in the slab models were allowed to relax during the geometry optimization to avoid the distortion of electronic property caused by constraints. We also tested placing protons on one side and both sides of the slab, and no obvious difference was observed in terms of spin density and charge density difference. Bader charge analysis was performed to estimate partial electronic charges on the adsorbed proton.[8-10]

Supplementary Tables

Supplementary Table 1 Catalyst characterization data

catalyst	Au wt.%	Reduction temperature (°C)	d_{Au} (nm)	SA (m^2/g)
2.7 nm-1.0%	1.0	275	2.7 ± 0.9	48
3.0 nm-2.3%	2.3	275	3 ± 1	48
2.9 nm-4.5%	4.5	275	2.9 ± 0.8	48
3.7 nm-4.5%	4.5	350	3.7 ± 1.1	44
4.2 nm-4.5%	4.5	425	4.2 ± 1.2	31

Supplementary Table 2. Catalyst particle analysis. %S and %P were calculated using the procedure described in the section **Particle Size Analysis.** Surface site density (Au_{sur}) and perimeter density density (Au_{per}) values were calculated using **Supplementary Equations S and 9**. The extracted Au_{sur} and Au_{per} site densities are also shown.

catalyst	%S	%P	Au_{sur} (μmol/g)	Au_{per} (μmol/g)
2.7 nm-1.0%	48	3.5	24.4	1.78
3.0 nm-2.3%	41	2.6	47.9	3.04
2.9 nm-4.5%	46	3.3	105.1	7.54
3.7 nm-4.5%	35	1.9	79.9	4.34
4.2 nm-4.5%	34	1.7	77.7	3.88

Supplementary Figures

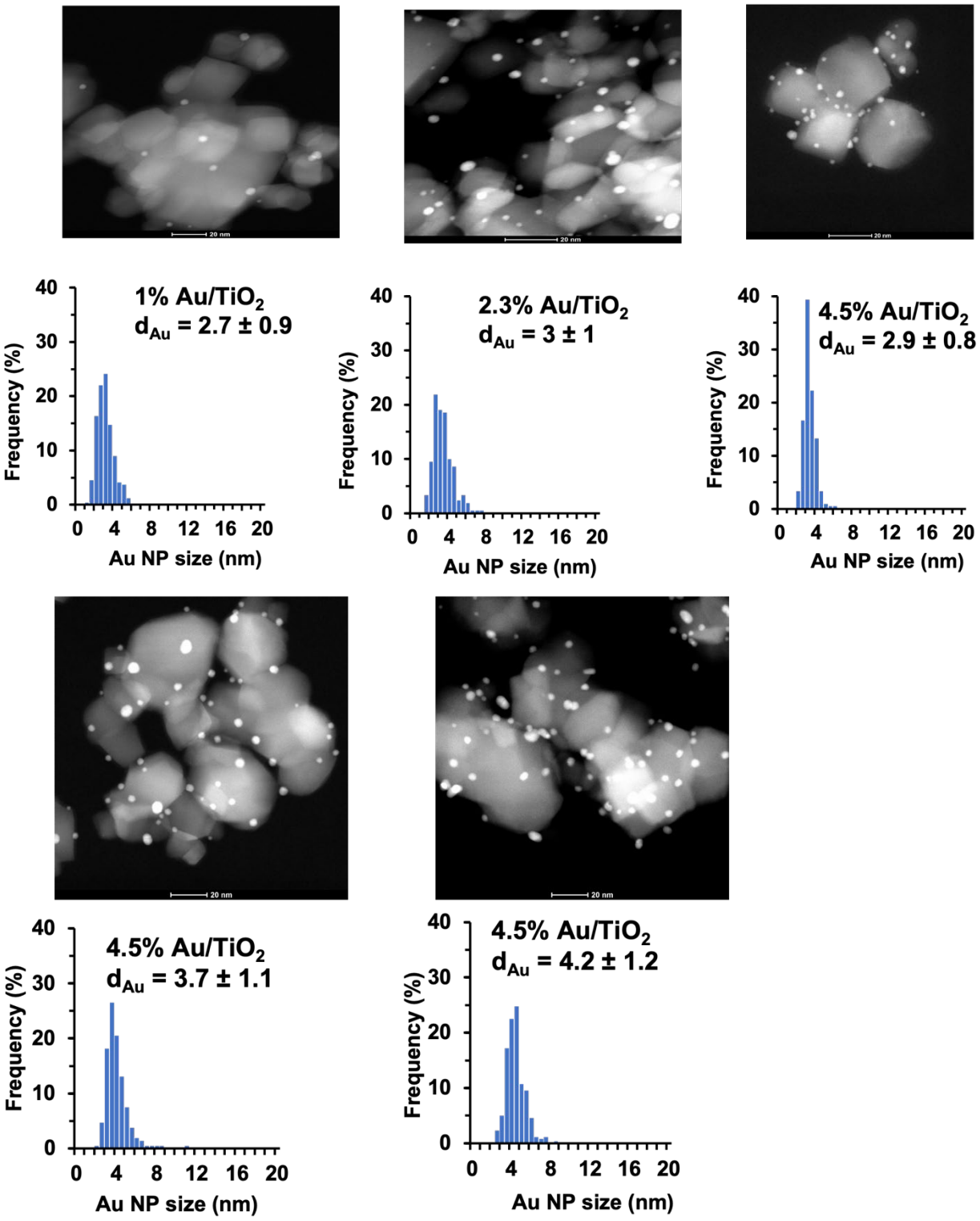

Supplementary Figure 1. STEM images of the catalysts (see Supplementary **Table 1**). Histograms and the average Au particle sizes are shown below the STEM images for each catalyst.

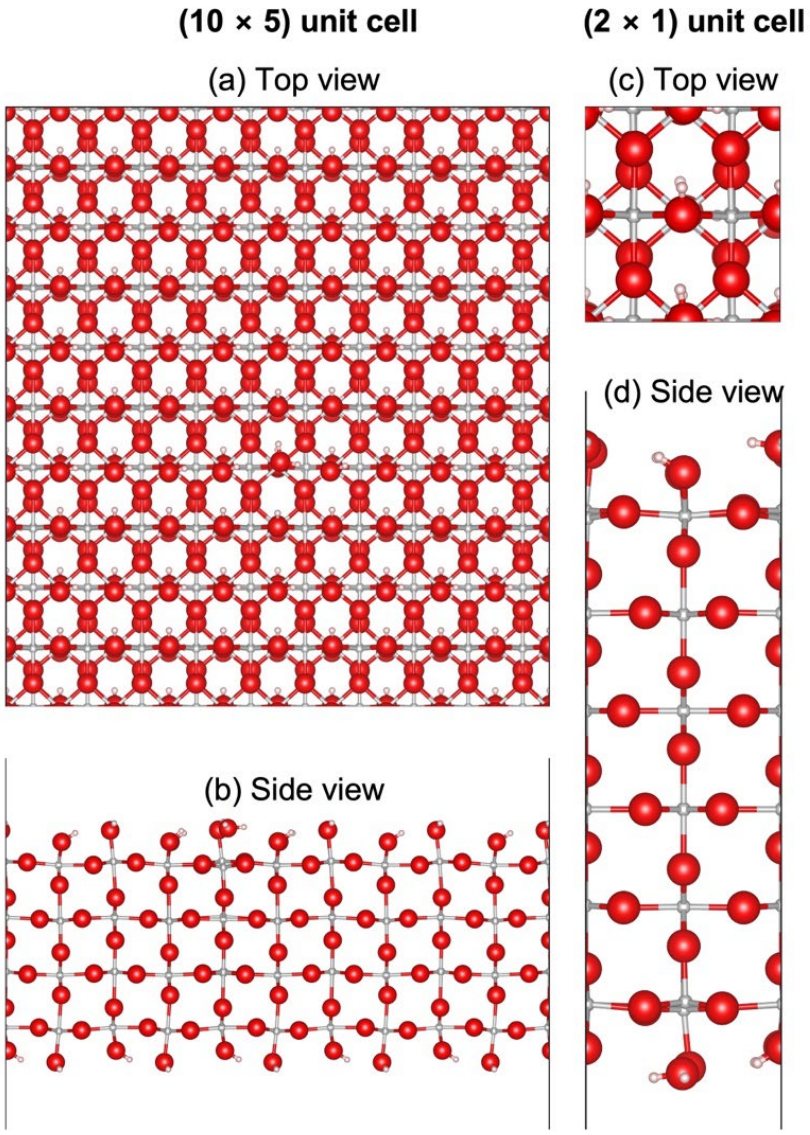

Supplementary Figure 2. Side and top views of the slab models used for calculating charge density difference and spin density of the adsorbed proton on TiO_2 surface at low (a and b) and high (c and d) coverages.

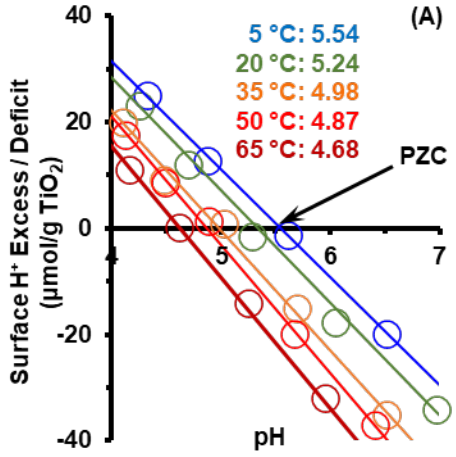

Supplementary Figure 3. Isoelectric point determinations for P25 titania at five different temperatures. The isoelectric point is the x-intercept of each fitted line.

Supplementary Discussion

Hydrogen adsorption is fast, but weak and reversible.

Infrared spectra collected during H_2 adsorption are shown in **Supplementary Figure 3A**; corresponding spectra collected during H_2 desorption are shown in **Supplementary Figure 3B**. The common features observed during adsorption include: (i) a positive absorbance feature at 3300 cm^{-1} attributed to protonated hydroxyls at the MSI ($_{MSI}TiOH_2^+$), which arise from heterolytic H_2 adsorption at the MSI; (ii) the appearance of a corresponding band at 1580 cm^{-1}, attributable to the scissoring mode of the $_{MSI}TiOH_2^+$ species; (iii) a negative absorbance feature at 3620 cm^{-1}, attributable to the loss of basic hydroxyls at the MSI ($_{MSI}TiOH$) upon protonation during H_2 adsorption; and (iv) a broad background absorbance (BBA) feature over the entire spectrum associated with electron addition to the support.

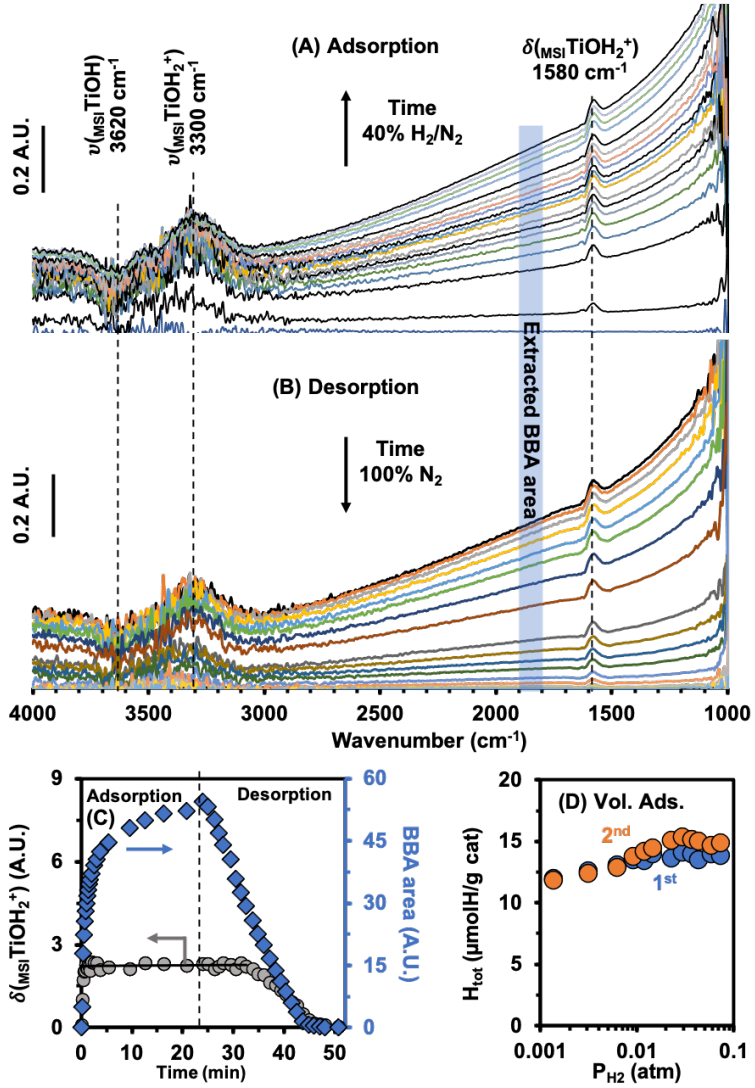

Supplementary Figure 3. (A) FTIR spectra of H_2 adsorption on the 2.9 nm-4.5% Au/TiO_2 catalyst. Spectra were recorded at 70 °C under 40% H_2/N_2. Spectra are difference spectra and referenced to the spectrum of the sample right before exposure to H_2. (B) Spectra recorded after H_2 was removed from the feed (100% N_2). (C) integrated area of the BBA (1800-1900 cm^{-1}) and the $_{MSI}TiOH_2^+$ δ_{HOH} band (1580 cm^{-1}) as a function of time extracted from the spectra in panel A and B. Note: time 0 min is the moment that H_2 was introduced to the chamber. (D) volumetric adsorption on the same catalysts at 60 °C.

These observations are all consistent with heterolytic dissociation of hydrogen at the MSI, as we recently reported. Briefly, the BBA feature can be calibrated to volumetric adsorption measurements and used for quantitative kinetic analyses. These studies indicated the MSI sites

are saturated in less than one minute after introducing H_2. The activation energy for H_2 adsorption was determined to be ~20 kJ/mol, which is considerably lower than previous estimates based on H-D exchange studies and similar to "fast" H_2 activation metals. Therefore, hydrogen activation at the Au-TiO_2 MSI is relatively fast and the kinetics of H_2 adsorption are unlikely to play a significant role in the thermodynamic measurements reported here.

Supplementary Figure 3B shows FTIR spectra recorded during the desorption process after removing H_2 from the feed. All the features created upon exposure to H_2 are eliminated 30 minutes after removing hydrogen from the feed. These adsorption / desorption experiments can be repeated multiple times; thus, H_2 adsorption is both fast and reversible (i.e. weak).

Supplementary Figure 3C shows the integrated BBA areas (in 1800-1900 cm^{-1} range, as shown with a blue box in panels A and B) and the $_{MSI}TiOH_2^+$ δ_{HOH} band (1580 cm^{-1}) as a function of time. The $_{MSI}TiOH_2^+$ δ_{HOH} band stabilizes in less than one minute while the BBA feature continues to increase after $_{MSI}TiOH_2^+$ δ_{HOH} band stabilization. In addition, the $_{MSI}TiOH_2^+$ δ_{HOH} band remains stable throughout the adsorption and most of the desorption process, until the latest stages of desorption. This indicates the $_{MSI}TiOH$ sites are almost immediately saturated with protons; the additional adsorption that gives rise to the continued growth in the BBA feature is consistent with the transfer of hydrogen atom equivalents to the support.

Supplementary Figure 3D shows a volumetric adsorption experiment on the same catalyst at 60 °C. The first adsorption isotherm was performed on a freshly reduced sample; the second isotherm was collected following 30 min of evacuation. The first and the second isotherms show essentially the same uptake indicating that adsorption is weak and reversible, in agreement with FTIR observations.

Note that there is no indication of water desorption upon hydrogen adsorption as (1) in the FTIR spectra there was no indication of a negative absorbance feature associate with water desorption in the difference spectra recorded at temperatures as high as 150 °C and (2) volumetric adsorption measurements would not show a pressure drop if there was a water desorption event per H_2 adsorption.

Hydrogen adsorbed at the MSI (HMSI)

We have recently reported a spectroscopic method to quantify the number of the reactive $_{MSI}TiOH$ using FTIR spectroscopy. In summary, as shown in **Supplementary Figure 4**, the response of the calibrated BBA signal can be used to quantify H_2 adsorption at any given time, most importantly the time at which the $_{MSI}TiOH_2^+$ δ_{HOH} band stabilizes. This marks saturation of MSI sites, and allowed for a spectroscopic determination of the number of active perimeter hydroxyls by determining the amount of hydrogen required to saturate the $_{MSI}TiOH_2^+$ δ_{HOH} band. We referred to this method as the FTIR titration. We have previously shown that there is approximately one reactive $_{MSI}TiOH$ per Au perimeter atom, regardless of metal loading or Au nanoparticle size.

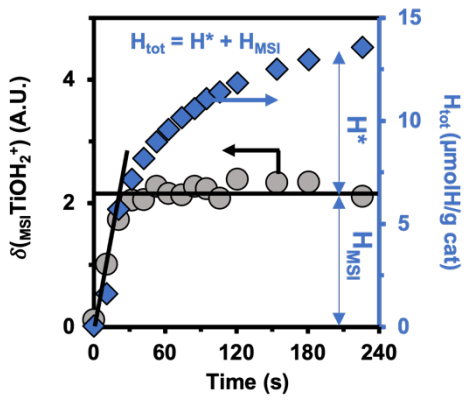

Supplementary Figure 4. FTIR titration method used for determining the H_{MSI} for the 2.9 nm-4.5% Au/TiO_2 catalyst at 70 °C and 0.4 atm H_2.

As shown above, the $_{MSI}TiOH_2^+$ bands are the first features formed upon H_2 adsorption and the last feature remaining at the end of desorption. This observation is consistent with a model where the MSI sites are first saturated with HAEs during the initial adsorption events and remain saturated throughout the adsorption process. We therefore conclude the additional HAEs must be added to the support. Thus, hydrogen adsorption (H_{tot}) on Au/TiO_2 has two components: (*i*) H_{MSI} and (*ii*) hydrogen adsorbed on the support away from the MSI. Hereafter we refer to these hydrogen atom equivalents (HAEs) as H*, to indicate HAEs are composed as dissociated protons on surface hydroxyls and electrons in surface conduction band states. While this can be considered a form of spillover hydrogen, the "spillover" term is not particularly descriptive given the likelihood there is little to no hydrogen adsorbed on the Au. The straightforward relationship between H_{tot}, H_{MSI}, and H* is shown in **Supplementary Equation (10)**.

$$H_{tot} = H_{MSI} + H^* \qquad (10)$$

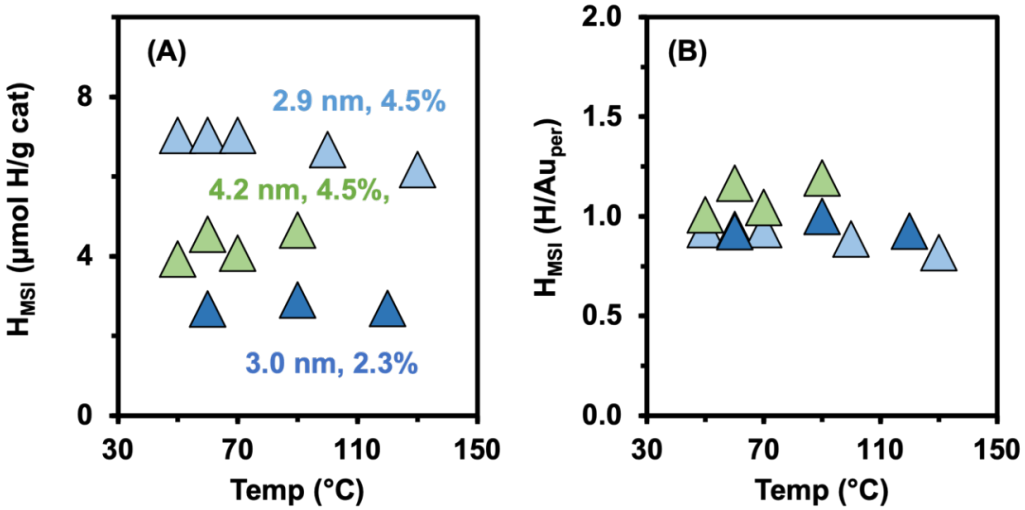

Supplementary Figure 5. The extracted H_{MSI} values using the FTIR titration method for the catalysts, c, d, and f under 40% H_2/N_2 at different temperatures. The corresponding FTIR titration figures for catalyst-d are shown in **Supplementary Figure 4.** (B) same data points as panel A, but shown in a different unit (H/Au_{per}).

As **Figures 1** and **2** in the main text show, H_{tot} is sensitive to temperature and H_2 pressure. We examined the sensitivity of H_{MSI} to the adsorption conditions. **Supplementary Figure 5** shows the extracted H_{MSI} values using FTIR titration method (**Supplementary Figure 4**) as a function of temperature for three catalysts. The extracted H_{MSI} values is almost constant for a given catalyst at different temperatures up to 100 °C. There is a slight decline at higher temperatures which is not surprising considering spill-over of these HAEs to the support. In addition, panel A shows difference in the H_{MSI} for different catalysts, which is not surprising considering these catalysts have different perimeter loadings. Panel B shows that H_{MSI} values normalized to the number of perimeter sites (H/Au_{per}) fluctuate around one for all these catalysts. These results show that the extracted H_{MSI} quantity is insensitive to temperature (up to 100 °C) for a given catalysts and only depends on the perimeter loading of the catalysts.

Based on these results, H_{MSI} can be determined directly using the FTIR titration method or estimated indirectly using STEM particle size analysis. The latter method assumes the 1:1 relationship between the H_{MSI} and Au_{per} sites. H_{MSI} values determined using both FTIR titration and STEM analysis methods show excellent agreement, which has several important implications. Most importantly, the bulk FTIR measurements validate the STEM data, which are always subject to image bias due to the necessarily small sample sizes.

Adsorption Isotherms

Supplementary Figure 6A shows the hydrogen adsorption isotherm on the 2.7 nm-1% Au/TiO_2 catalyst at 90 °C. **Supplementary Figure 6B** shows the same data set, but with P_{H2} values plotted on a logarithmic scale to more easily visualize the data across the pressure range, which varies by three orders of magnitude. The green data points are associated with the measured quantities using volumetric adsorption; the gray data points show the uptake values measured using the calibrated BBA signal.

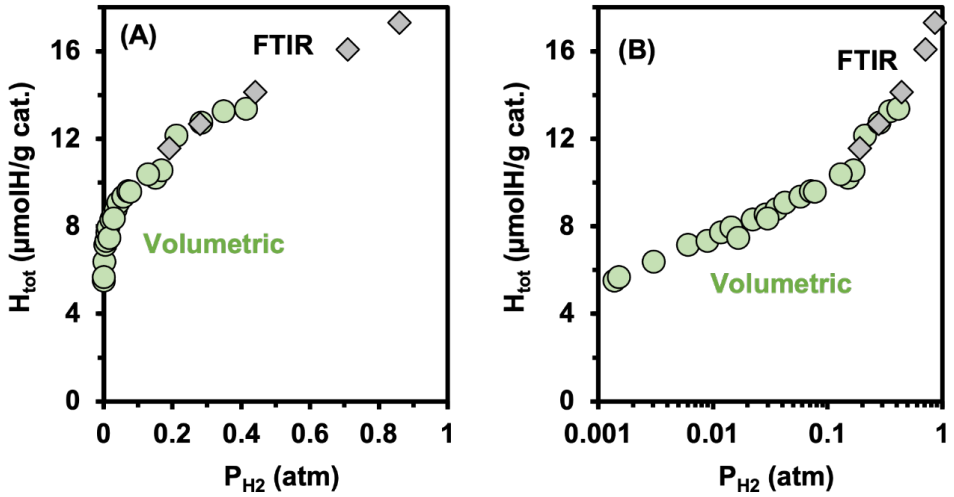

Supplementary Figure 6. (A) Hydrogen adsorption isotherm on the 1%-2.7nm Au/TiO_2 catalyst at 90 °C. green circles show values measured directly via volumetric adsorption; gray diamonds show the uptake measured using the calibrated BBA signal. (B) same data set as panel A, but P_{H2} is shown in logarithmic scale.

Due to the relatively small number of adsorption events and very weak adsorption, volumetric adsorption experiments showed large measurement errors at pressures above ~0.5 atm. We therefore limited our volumetric measurements to pressures less than 0.5 atm. FTIR experiments,

on the other hand, have few interferences and are more easily able to distinguish small changes in adsorption at higher pressures. We conveniently achieve hydrogen pressures as low as 0.15 atm in the FTIR cell without the need for serial dilution. Accordingly, we made FTIR measurements over 0.15-0.9 atm H_2.

The two measurement techniques (FTIR and volumetric) overlap in the 0.15-0.5 atm range; this overlapping range was used to calibrate the BBA signal against volumetric adsorption. After calibrating the BBA signal, the high pressure data points are reliably similar to the volumetric adsorption as shown by grey diamonds in **Supplementary Figure 6**. For clarity, further isotherms do not differentiate between the FTIR and volumetric adsorption data points, as they are internally calibrated.

Langmuir analysis

The Langmuir model, which describes equilibrium adsorption on energetically uniform surface sites, is by far the most common starting point for understanding adsorption on catalyst surfaces:

$$QA = \frac{QA^{max} K P_{H2}}{1 + K P_{H2}} \tag{11}$$

$$\frac{1}{QA} = \frac{P_{H2}}{QA^{max} K P_{H2}} + \frac{1}{K Q A^{max}} \tag{12}$$

$$\frac{P_{H2}}{QA} = \frac{P_{H2}}{QA^{max}} + \frac{1}{QA^{max}} \tag{13}$$

where K is the equilibrium constant, QA is the quantity adsorbed at each pressure point and QA^{max} is the maximum quantity adsorbed extracted from linearized Langmuir plots (Equation B). Note that QA^{max} is not a true maximum adsorption capacity and additional non-Langmuirian and coverage-dependent adsorption continues as the H_2 pressure increases, as shown in **Supplementary Figure 7.**

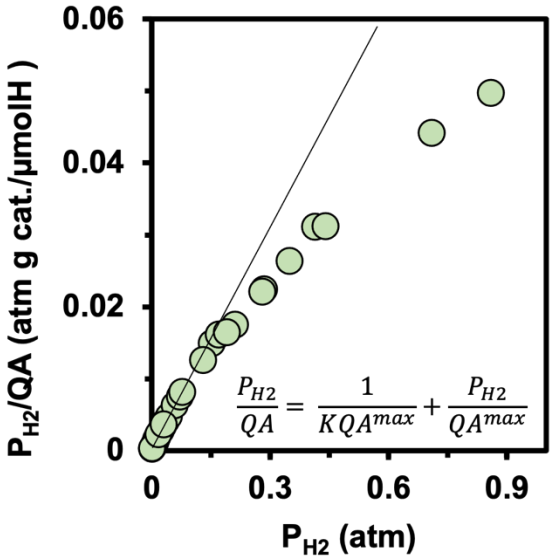

Supplementary Figure 7. Linearized Langmuir plot for hydrogen adsorption on the 2.7 nm-1% Au/TiO_2 catalyst at 90 °C. The black line shows the linear fit to the data points in the 0.001-0.1 atm range.

Supplementary Figure 7 shows the results of applying the Langmuir model to a representative data set (2.7 nm-1% Au/TiO_2, 90 °C), which covers three orders of magnitude in P_{H2}. The full isotherm does not fit linearized forms of the Langmuir model (**Supplementary equations 12 and 13**), indicating more complex coverage-dependent adsorption processes are at work. While the Langmuir model cannot describe all this data, the Langmuir assumption of coverage-independent adsorption does a good job of describing the adsorption over smaller pressure ranges, indicating relatively consistent adsorption energetics over smaller pressure ranges. The linear behavior is not specific to a particular pressure range and Langmuir's assumptions are reasonable within any sufficiently narrow pressure range for this data.

In addition, **Supplementary Figure 8** shows that H_{tot} exceeds the number of perimeter sites even at the lowest H_2 pressures used in this study. This is consistent with our FTIR observations that the MSI sites are immediately saturated upon exposure to H_2. Therefore, the adsorption pressure dependence of the isotherms is entirely due to the pressure dependence of H* and we focus on the H* values in the Langmuir analysis (see below).

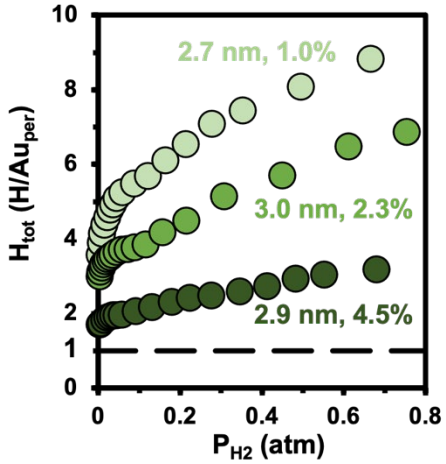

Supplementary Figure 8. Hydrogen adsorption isotherms of three catalysts at 90 °C.

To quantitate the temperature effects, we evaluated a narrower pressure range where the changes adsorption energy are < 15% (0.01-0.04 atm,~25 Torr; highlighted in **Supplementary Figure 8**). **Supplementary Figure 9A** shows representative plots for several catalysts at 30 °C; **Supplementary Figure 9B** shows data from the temperature study in **Figure 1A (main text)**. This narrower pressure range is well described by the Langmuir model, which provides two important adsorption descriptors: the equilibrium constant (K_P^*) and the measured "maximum" surface concentration ($_{surf}C_P^*$) where P indicates the middle of the pressure range. The $_{surf}C_P^*$ values therefore report on the number of adsorption sites associated with adsorption energies accessible at a given pressure. By definition, adsorption sites populated at higher pressures (i.e. weaker adsorption sites) are not included in this analysis, but can be evaluated using a different pressure range. **Supplementary Tables 3-6** compile the extracted adsorption parameters for 5 catalysts at 30, 60, 90, and 120 °C. Both the $_{surf}C_{P25}^*$ and K_{25}^* values are remarkably consistent across the catalysts, indicating the amount of H* (at a given temperature and pressure) is independent of Au particle size or loading and is always the same within very reasonable measurement errors.

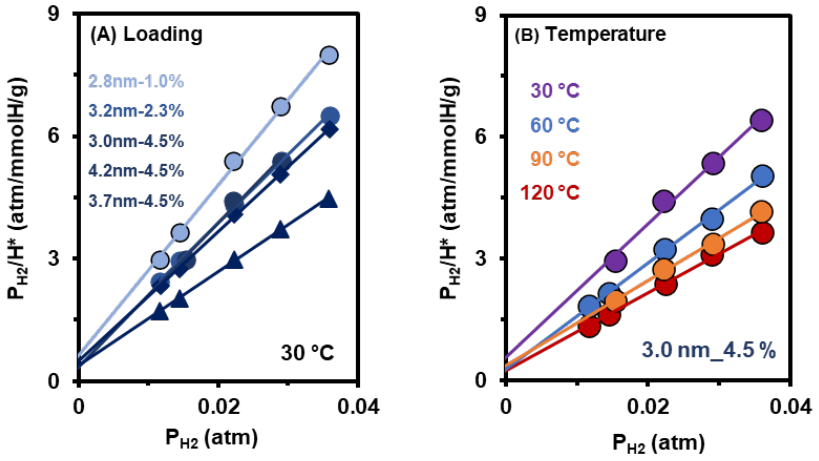

Supplementary Figure 9. Representative linear Langmuir plots for (A) 5 catalysts at 30 °C and (B) a 4.5 % Au/TiO_2 catalyst at 4 different temperatures. The extracted values are summarized in Table below. Comparable analyses were performed on all 5 catalysts at all 4 temperatures (available in the SI).

Supplementary Table 3. Extracted Langmuir values at 30 °C.

Catalysts	${}_{surf}C^*_{P25}$ (µmolH*/g cat.)	K^*_{25} (atm^{-1})	ΔG_{25} (kJ/mol)
2.7 nm-1.0%	4.8	326	-14.3
3.0 nm-2.3%	5.9	332	-14.4
2.9 nm-4.5%	6.1	290	-14.0
3.7 nm-4.5%	8.7	301	-14.1
4.2 nm-4.5%	6.3	325	-14.3
Ave ± stdv	6.4 ± 1.4	320 ± 30	-14.2 ± 0.1

Supplementary Table 4. Extracted Langmuir values at 60 °C.

Catalysts	${}_{surf}C^*_{P25}$ (µmolH/g cat.)	K^*_{25} (atm^{-1})	ΔG_{25} (kJ/mol)
2.7 nm-1.0%	6.0	335	-14.4
3.0 nm-2.3%	6.9	332	-14.4
2.9 nm-4.5%	7.6	474	-15.3
3.7 nm-4.5%	9.5	417	-14.9
4.2 nm-4.5%	9.0	372	-14.7
Ave ± stdv	7.8 ± 1.5	386 ± 60	-14.7 ± 0.4

Supplementary Table 5. Extracted Langmuir values at 90 °C.

Catalysts	${}_{surf}C^*_{P25}$ (µmolH/g cat.)	K^*_{25} (atm^{-1})	ΔG_{25} (kJ/mol)
2.7 nm-1.0%	7.1	312	-14.2
3.0 nm-2.3%	7.5	271	-13.9
2.9 nm-4.5%	9.3	292	-14.1
3.7 nm-4.5%	10.3	348	-14.5
4.2 nm-4.5%	9.4	347	-14.5
Ave ± stdv	8.7 ± 1.4	314 ± 34	-14.2 ± 0.3

Supplementary Table 6. Extracted Langmuir values at 120 °C.

Catalysts	${}_{surf}C^*_{P25}$ (μmolH/g cat.)	K^*_{25} (atm^{-1})	ΔG_{25} (kJ/mol)
2.7 nm-1.0%	7.3	285	-14.0
3.0 nm-2.3%	7.8	306	-14.2
2.9 nm-4.5%	10.4	417	-14.9
3.7 nm-4.5%	10.4	316	-14.3
4.2 nm-4.5%	10.1	327	-14.3
Ave ± stdv	9.2 ± 1.5	330 ± 51	-14.3 ± 0.4

A van't Hoff analysis (**Supplementary Figure 10**) yields a thermoneutral enthalpy of ΔH_{25} = 0 ± 2 kJ/mol and a ΔS_{25} value of +49 ± 6 J/mol K, indicating the H* adsorption is entropically favorable.

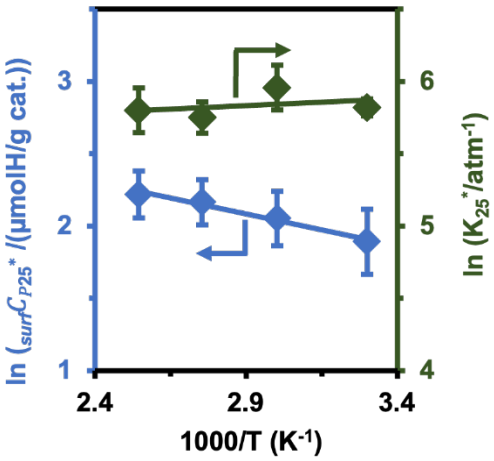

Supplementary Figure 10. Van't Hoff analysis using the average extracted Langmuir parameters as a function of temperature. The symbols are average of 5 data points measured over 5 different catalysts (**Supplementary Tables 3-6**) and the error bars represent the standard deviations of all those measurements.

Adsorption energies (progressive Langmuir method):

As shown above, while the broader adsorption isotherm is clearly not Langmuirian, the Langmuir model does a good job of describing the data over sufficiently small pressure ranges (where the adsorption energy is relatively constant). Coverage-dependent adsorption energies can therefore be evaluated using Langmuir equilibrium constants (K) determined over small pressure ranges. For consistency, we minimized the pressure range as much as possible, extracting the apparent equilibrium constant at each adsorption point using only two neighboring data points (one on each side, see **Supplementary Figure 11**).

The extracted Langmuir equilibrium constants at 90 °C, plotted as a function of the amount of H* on the catalyst for the 1% Au/TiO_2 catalyst are shown in **Supplementary Figure 12**. The extracted equilibrium constants change substantially with adsorbed H*, ranging from 1000 atm^{-1} to less than 10 atm^{-1}. **Supplementary Figure 12B** shows determined values for ΔG_{ads} as a function of H*; these values approach 1 as H* coverage increases, consistent with the weak nature of the adsorption. The ΔS values shown in **Supplementary Figure 12-C** were calculated considering a ΔH = 0, based on the Van't Hoff analysis shown in **Supplementary Figure 11**.

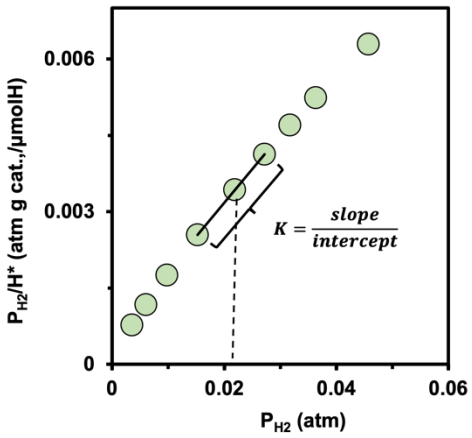

Supplementary Figure 11. The sliding method used to extract the adsorption equilibrium constant (K) values for each adsorption point. Based on the Langmuir model, $K = \frac{slope}{intercept}$. The data correspond to H_2 adsorption on the 1% Au/TiO_2 catalyst at 90 °C.

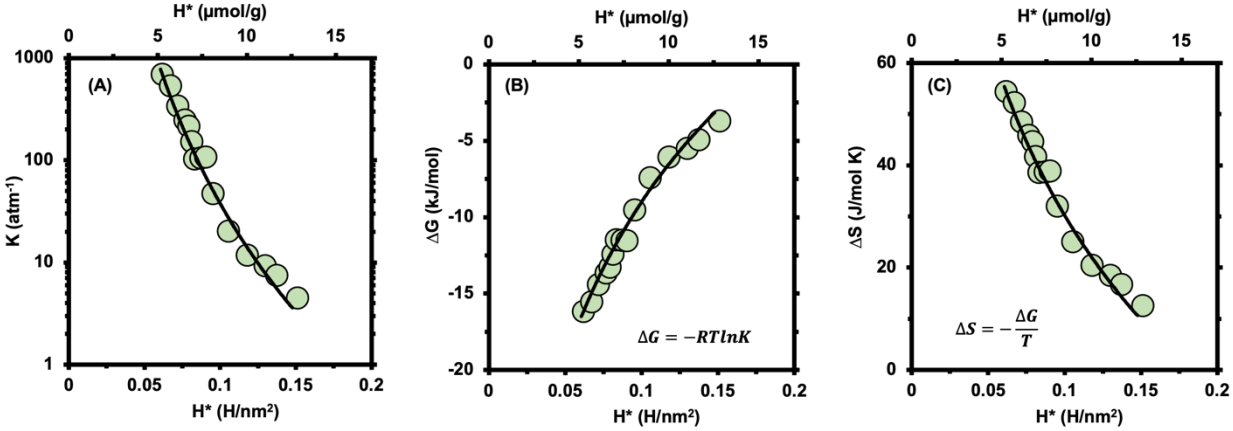

Supplementary Figure 12. (A) Langmuir equilibrium constants, (B) Gibbs free energies, and (C) entropy of adsorption as a function of H* for the 1% Au/TiO_2 catalyst at 90 °C. The lines are added to guide the eye.

Two-Site Langmuir Model

The H* adsorption data can also be described by a two-site Langmuir adsorption model. **Supplementary Figure 13** shows the data in **Figure 1A** fitted to a site density and adsorption equilibrium constant for strong and weak adsorption sites (i.e. 4 independent parameters: K_{str}, D_{str}, K_{wk}, D_{wk}). Extracted values are shown in **Supplementary Table 7**. The temperature dependence of the fitted parameters are plotted in **Supplementary Figures 14 and 15**.

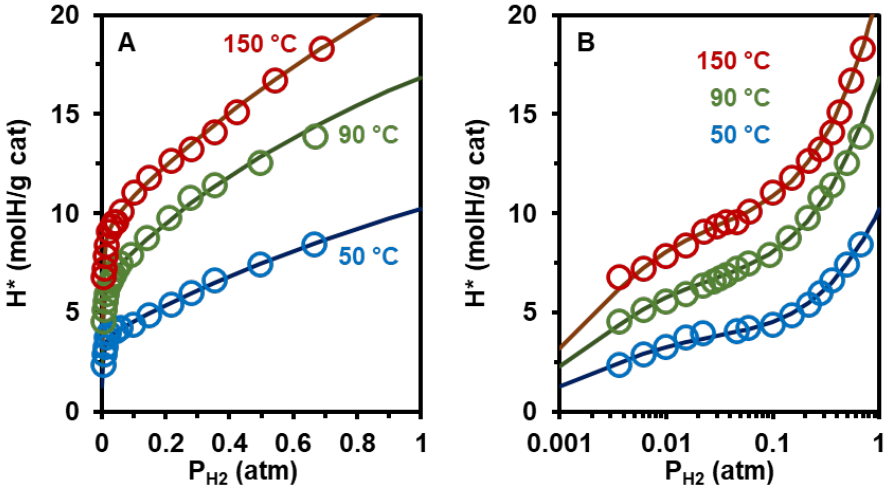

Supplementary Figure 13. H* adsorption isotherms and two-site Langmuir fits for 1.0%-2.8 nm Au/TiO_2 plotted on **(A)** linear and **(B)** logarithmic P_{H2} scales.

Supplementary Table 7. Fitted Two-Site Langmuir Parameters.

	Parameter	50 °C	90 °C	150 °C	units
Strong adsorption sites	D_{str}	3.8	6.8	9.5	μmol H*/g cat
	K_{str}	520	430	510	atm^{-1}
	ΔG_{str}	-16.8	-16.3	-16.8	kJ/mol
Weak adsorption sites	D_{wk}	26	24	37	μmol H*/g cat
	K_{wk}	0.33	0.63	0.45	atm^{-1}
	ΔG_{wk}	3.0	1.3	2.2	kJ/mol
Total sites	D_{tot}	30	31	38	μmol H*/g cat

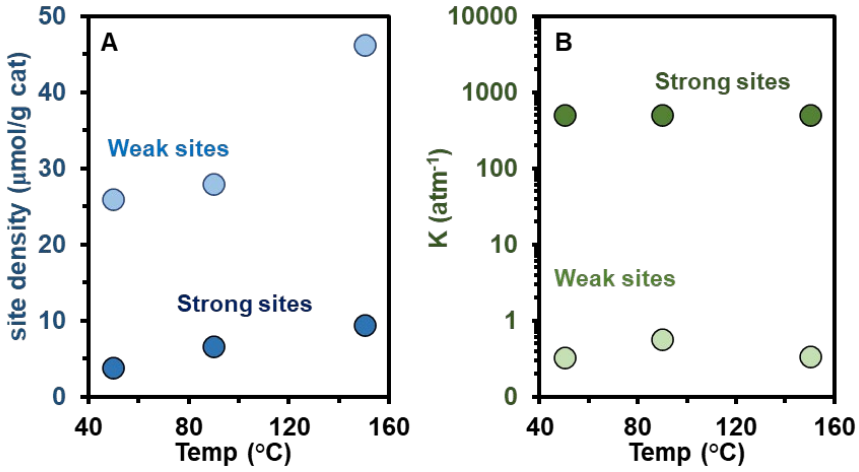

Supplementary Figure 14. Temperature dependence of **(A)** site density and **(B)** adsorption equilibrium constant (K) or parameters extracted from the two-site Langmuir model.

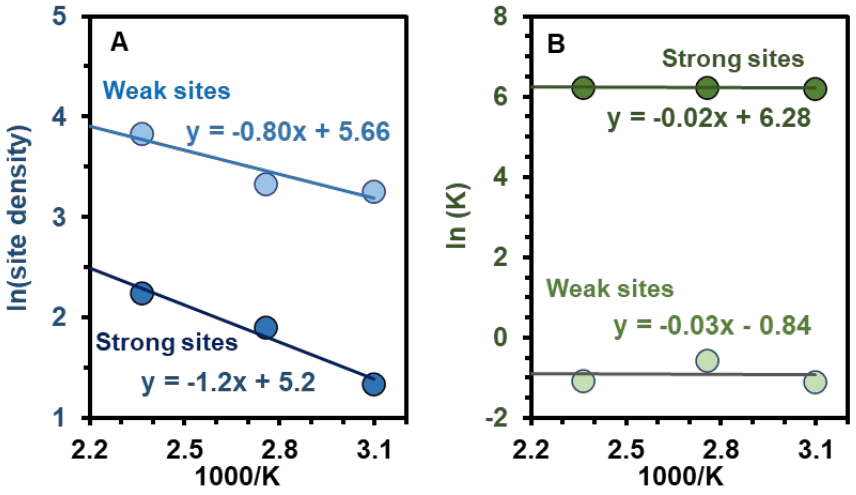

Supplementary Figure 15. Van't Hoff analysis of extracted **(A)** site density and **(B)** adsorption equilibrium constant values extracted from the two-site Langmuir model.

Results from the two-site Langmuir model agree broadly with the progressive Langmuir treatment. Both treatments of the H* adsorption data show an increase in site density (both strong and weak) as temperature increases (**Supplementary Figure 14**). Similarly, the Van't Hoff analyses both show essentially thermoneutral adsorption enthalpy (**Supplementary Figure 15**). We note the strong adsorption sites in the two-site model are extremely similar thermodynamics to the collected at 25 torr (**Figure 4F** in the main text and **Supplementary Figure 10** above); the total number of sites is essentially the same and the equilibrium constants vary by less than a factor of two. It is also noteworthy the two-site model requires weak adsorption sites with both very weak adsorption enthalpy and a slightly unfavorable entropy of adsorption.

The two-site and progressive Langmuir models approach the problem of a coverage-dependent equilibrium adsorption constant from opposite ends. The two-site model treats the system as if there are two specific sites with fixed adsorption energies. It then attributes the observed changes in adsorption energetics to a weighted average of the adsorption sites available at a given pressure. The progressive approach makes no requirements on the number of sites or the adsorption energetics but allows the adsorption energetics to vary with coverage. This is similar to the approach in the Temkin adsorption model, without the limitation that adsorption should vary linearly with coverage.

Both models indicate the number of adsorption sites increases with increasing temperature. The two-site model is attractive in its relative simplicity and familiar conceptual framework. The two sites would, ostensibly, be two different types of surface zwitterions, perhaps associated with different local arrangements on the surface. However, given the very low surface concentrations of these sites, they would likely be very difficult to isolate and characterize.

The progressive Langmuir approach allows the adsorption equilibrium to vary directly due to changes in the translational and configurational entropy. This allows the number of possible adsorption sites to remain some-what ill-defined and potentially very large. We believe this is appropriate for the system as it is difficult to know exactly how many surface zwitterions are present, much less their location. Additionally, protons are rapidly exchanged across the surface; while it is conceptually more comfortable to think of a specific site, rapid exchange may make reality more complicated. This coincides with the broader impact of configurational entropy, as of all possible surface proton configurations impact the surface's ability to stabilize H*.

At present both treatments do a good job of describing individual isotherms, so neither can be discounted. However, the two-site model has a few inconsistencies with the aggregate data. First, while the number of strong sites clearly increases with temperature, this is less clear for the weak adsorption sites. The model finds the weak sites density to be ~5x greater than the strong site density, so the weak sites dominate the overall site density. Consequently, the total number of aggregate sites increases from 30 to 38 μmol H*/g cat, approximately 25%. The translational entropy model in Figure 6B indicates the total site density shifts from ~0.5 to ~0.2 μmol H*/g cat – roughly a factor of four. So, while the order of magnitude of the two-site model is reasonable, the fitted increase in the number of sites as the temperature increases is less consistent with the entropic explanation for H* adsorption. Accordingly, while certainly see the value in and cannot rule out and the two-site model, we believe the progressive treatment does a slightly better job of describing the system.

Entropy calculations:

We follow Vannice's two-step dissociative adsorption procedure for calculating the ΔS_{ads}, which involves gas-phase dissociation followed by atomic adsorption on the surface:

$$\Delta S_{ads} = \Delta S_{dissociation} + 2\Delta S_{adsorption}$$

$\frac{1}{2}$ $H_{2\,(g)} \rightleftharpoons H_{(g)}$ $\qquad \Delta S^0_{dissociation} = 109 \pm 8 \frac{J}{mol\ H_2} K$ (14)

$H_{(g)} \rightleftharpoons H^*$ $\qquad \Delta S_{adsorption}(\theta) = S_{H^*}(\theta) - S^0_H(g);\ S^0_H(g) = 115 \frac{J}{mol\ H}\ K$ (15)

We note a single-step process using the standard state gas phase entropy of $H_{2\,(g)}$ yields essentially the same result.

The total entropy of adsorption depends on the entropy of the adsorbed species. This value has a strong coverage dependence:

$$\Delta S_{adsorption}(\theta) = S_{H^*}(\theta) - S^0_H(g) \quad (16)$$

The experimental $S_{H^*}(\theta)$ values were calculated using the extracted $\Delta S_{ads}(\theta)$ values, **Figure S11-C**. In general, the entropy of adsorbed species is described by equation (S16),

$$S_{H^*}(\theta) = S_{H^*,tr}(\theta) + S_{H^*,config}(\theta) + S_{H^*,vib}(\theta) + S_{H^*,electron}(\theta) \quad (17)$$

where

$S_{H^*,tr}$ is the translational entropy

$S_{H^*,config}$ is the configurational entropy

$S_{H^*,vib}$ is vibrational entropy

$S_{H^*,electron}$ is electronic entropy

This model evaluates the individual contributions of each component to the total adsorbate entropy. For adsorbed hydrogen atoms on semiconducting supports, the adsorbates move freely on the surface; we therefore treat the adsorbate H* with the 2D ideal gas model. In this case, the

vibrational and electronic entropies are relatively small and are unlikely to significantly change with temperature. As argued by Vannice et al., each vibrational mode contributes about 1 e.u. (4.184 J/mol K) to the total entropy of the adsorbate and an adsorbed atom can have up to 3 vibrational modes. Therefore, the vibrational entropy of the adsorbed hydrogen atoms ($S_{H^*,vib}$) should be less than 12 J/mol K. We therefore focus our attention on translational and configurational entropy contributions, employing Vannice and Campbell's treatments.

Translational entropy

The $S_{H^*,tr}$ is calculated with **equation (1)**, main text. Note, at a fixed temperature, $S_{H^*,tr}$ depends only on the area available to each adsorbate (parameter a) and is independent of the number of available adsorption sites. This is particularly important for the adsorption on complex surfaces where the total number of adsorption sites is not known and/or could change with the experimental conditions.

The Vannice and Campbell treatments of translational entropy appear to be considerably different. Vannice's description[11] is described in **Supplementary Equation 18**:

$$S_{tr} = Rln(MTa) + 275\frac{J}{mol\ K} \tag{18}$$

Where M is molar mass (g/mol), T is absolute temperature (K), a is the area available to each adsorbate (cm^2/atom), which is simply the inverse of the H^* site density. This treatment requires expressing α in units of cm^2 and treating the MTα term inside the natural logarithm as a unitless parameter.

Campbell uses a more complete and clearly recognizable 2D version of the Sackur-Tetrode equation:[12,13]

$$S_{tr} = Rln\left(\frac{\left(\frac{2\pi mkT}{h^2}\right)e^2}{\left(\frac{N_A}{A}\right)}\right) \tag{19}$$

Where R is gas constant, k is Bolzmann's constant (1.38×10^{-23} m^2kg/s^2K), h is Planck's constant (6.626×10^{-34} m^2kg/s), N_A is Avogadro's number (1/mol), M is molar mass (g/mol), T is absolute temperature (K), α is the area available to each adsorbate (nm^2/atom), which is simply the inverse of the H^* site density.

As we show in equations S19-S21,Campbell's treatment reduces to the same equation employed by Vannice. For clarity, and to eliminate the non-traditional treatment of units in the natural logarithm, we define the β constant: β = 2.42328 (mol/g·K·nm^2) and note the 10^{21} in equation S20 results from combining the fundamental constant units. We note α can be expressed in units of m^2/adsorbate (derived more directly from typical surface area measurements), resulting in simple change of the β value to 2.42328×10^{18} (mol/ g·K·m^2).

$$S_{tr} = Rln\left(\frac{\left(\frac{2\pi mkT}{h^2}\right)e^2}{\left(\frac{N_A}{A}\right)}\right) = Rln\left(\left(\frac{2\pi mkT}{h^2}\right)e^2a\right) \tag{20}$$

$$= Rln\left(\frac{2\pi ke^2}{10^{21}N_Ah^2} * MT\alpha\right) \tag{21}$$

$$= Rln(\beta MTa) \tag{22}$$

Supplementary Figure 16 shows both methods plotted independently; they are clearly identical treatments.

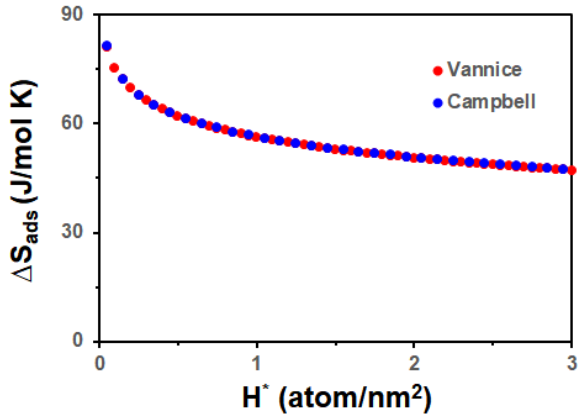

Supplementary Figure 16. Calculated translational entropy from equations in Vannice's and Campbell's treatments.

Comparison with adsorption on metal surfaces

Readers accustomed with adsorption on metal surfaces might find the idea of entropy driven adsorption shocking. However, the difference between the adsorption of hydrogen atom equivalents on the high surface area oxide surfaces is distinct from direct adsorption on the metal surfaces. Vannice et al., argued that $\Delta S°_{ads}$ should be favorable for dissociative adsorption, considering θ = ½ as the standard state and a site density of 10 sites/nm^2 (5 atoms/nm^2 at the standard state). Note that this corresponds to 0.2 nm^2 per adsorbate. We have used the same method here as Vannice et al. and we also calculated $\Delta S_{(tr)}$ = - 47 J/mol K for 5 atoms/nm^2.

While a site density of 10 sites/nm^2 is appropriate for adsorption on metal surfaces, the site density for more complex sites such as hydroxyls and/or defect sites on oxide surfaces could be smaller. For a given adsorbate at a fixed temperature, $S_{H^*,tr}$ is only a function of the area available to each adsorbate 'a', see **equation (1)** of main text.

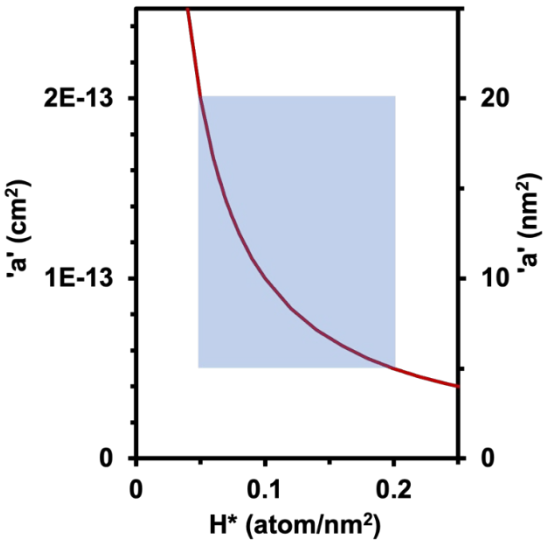

Supplementary Figure 17. Area available to each adsorbate as a function of number of adsorbates/nm^2. The blue shade shows the number of adsorbate per unit area of the surface measured in this work for Au/TiO_2 catalysts in 50-150 °C range. Within our measurement window, there is 5-20 nm^2 net area available.

Supplementary Figure 17 shows the area available to each adsorbate as a function of quantity adsorbed (atom/nm^2). The range of values relevant to the experimentally measured

quantities in this work is highlighted with a blue box. Note that there are 5-20 nm^2 net area available for each adsorbate within our experimentally measured values; for these values, using the same theory as Vannice et al., entropy driven adsorption is certainly plausible.

In general, the large area available per adsorbed species along with the dynamic nature of the adsorption sites distinguish adsorption of hydrogen atom on the high surface area oxide surfaces via spillover from direct adsorption on the metal surfaces. It is of fundamental and practical interest to note that while the total quantity adsorbed is comparable with the adsorption on the metal surfaces, adsorption on the complex sites/surfaces such as hydroxyls of TiO_2 can show very different behaviors. This is because the lower site density can be compensated with their higher surface area. Therefore, although the total quantity adsorbed is comparable with the adsorption on the metal surfaces, they can show unusual behaviors because they operate in different regimes not commonly (easily) measurable for adsorption on metal surfaces.

Configurational entropy

The configurational entropy is calculated with equation (2), main text. Note, determining the configurational entropy requires knowing the total number of possible configurations in order to determine a fractional coverage. The configurational entropy will therefore be impacted by the protonation state of the surface as well as the surface's ability to stabilize the added protons and electrons. These contributions, and their changes with temperature are presently unknown. We therefore considered several possible values for the net number of adsorption sites. These values are arbitrary and chosen to show the possible effects of increasing the number of sites; they should not be considered as determinations of the number of possible adsorption sites.

Supplementary Figure 18 shows the configurational entropy values calculated using four net adsorption sites densities. The agreement between the calculated values and the experimentally measured values after considering both the translational and configurational entropies (**Figure 6B** of Main text) is consistent with a picture where the total number of adsorption sites increases with temperatures.

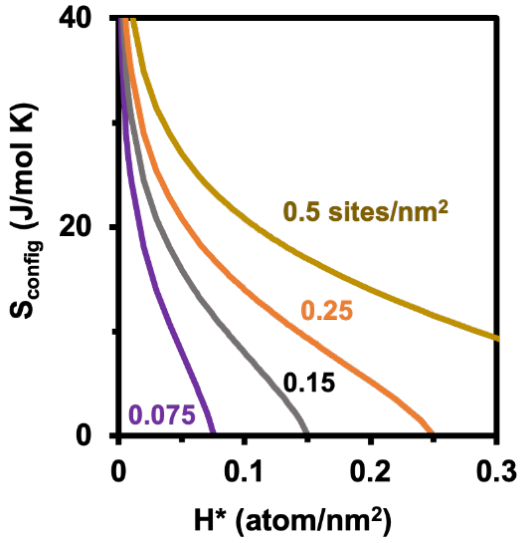

Supplementary Figure 18. Configurational entropies calculated as a function of H* using **Equation (2)** of main text for different arbitrary maximum number of adsorption sites (ns values).

Conduction Band Filling

We evaluated the potential role of temperature induced changes to the electron distribution in the titania valence and conduction bands. A freely available calculator is available at: http://hyperphysics.phy-astr.gsu.edu/hbase/Solids/Fermi.html; results are plotted in **Supplementary Figure 19**.

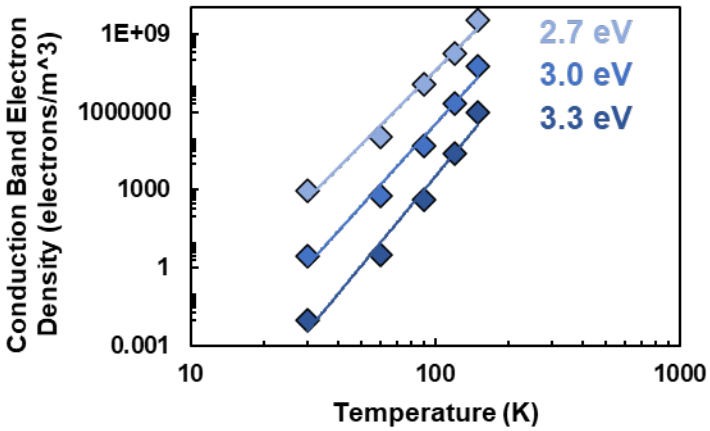

Supplementary Figure 19. Semiconductor conduction band electron density vs. temperature. Bandgap values centered around reported values for titania were used. All bandgap values have a similar temperature dependence

Over the range of temperatures used in the adsorption experiments (30-150 °C), the conduction band electron density increases by 6-7 orders of magnitude. This is a significantly larger change than the observed increase in the number of possible adsorption sites (roughly a factor of four based on the fits in **Figure 6B** in the main text). This is a significant size mismatch, so changes in conduction band population alone cannot account for the increases in adsorption site density with temperature.

More importantly, the increasing conduction band population with increasing T is expected to destabilize the H* electrons added to the system rather than promote H* adsorption. This is likely to decrease the overall H* adsorption energy rather than increase the number of adsorption sites. This is consistent with a smaller change in the number of H* adsorption sites than would be expected based on changes to surface zwitterion concentration alone.

Surface Zwitterion Formation

The zwitterion surface concentration can be estimated by extrapolating data from the aqueous titrations as follows:

$$ {}_{a}TiOH + {}_{b}TiOH \rightleftharpoons {}_{a}TiO^{-} + {}_{b}TiOH_2^{+} \quad (23)$$

$$ K_{ZI} = \frac{[aTiO^{-}][bTiOH_2^{+}]}{[aTiOH][bTiOH]} = \left(\frac{[ZI]}{[aTiOH]}\right)\left(\frac{[ZI]}{[bTiOH]}\right) \quad (24)$$

$$ {}_{a}TiOH + H_2O \rightleftharpoons {}_{a}TiO^{-} + H_3O^{+} \quad (25)$$

$$ {}_{b}TiOH + H_2O \rightleftharpoons {}_{b}TiOH_2^{+} + OH^{-} \quad (26)$$

$$ {}_{a}TiOH + {}_{b}TiOH + 2\,H_2O \rightleftharpoons {}_{a}TiO^{-} + {}_{b}TiOH_2^{+} + H_3O^{+} + OH^{-} \quad (27)$$

$$K_a K_b = \frac{[aTiO^-][bTiOH_2^+][H_3O^+][OH^-]}{[aTiOH][bTiOH]} \quad (28)$$

$$\frac{K_a K_b}{K_w} = \frac{[aTiO^-][bTiOH_2^+]}{[aTiOH][bTiOH]} = K_{ZI} \quad (29)$$

$$\frac{K_a[aTiOH]K_b[bTiOH]}{K_w} = [ZI]^2 \quad (30)$$

Surface $_a$TiOH and $_b$TiOH concentrations are estimated at 90 and 150 °C by extrapolating the data in **Figure 8a**; K_a and K_b values are estimated at 90 and 150 °C by extrapolating the data in **Figure 8b**.

Supplementary References

1 Cargnello, M. *et al.* Control of Metal Nanocrystal Size Reveals Metal-Support Interface Role for Ceria Catalysts. *Science* **341**, 771-773 (2013). https://doi.org:10.1126/science.1240148

2 Kresse, G. & Furthmuller, J. Efficiency of ab-initio total energy calculations for metals and semiconductors using a plane-wave basis set. *Comput. Mater. Sci.* **6**, 15-50 (1996). https://doi.org:10.1016/0927-0256(96)00008-0

3 Kresse, G. & Furthmueller, J. Efficient iterative schemes for ab initio total-energy calculations using a plane-wave basis set. *Phys. Rev. B: Condens. Matter* **54**, 11169-11186 (1996).

4 Kresse, G. & Hafner, J. Ab initio molecular dynamics of liquid metals. *Phys. Rev. B: Condens. Matter* **47**, 558-561 (1993).

5 Wellendorff, J. *et al.* Density functionals for surface science: exchange-correlation model development with Bayesian error estimation. *Phys. Rev. B: Condens. Matter Mater. Phys.* **85**, 235149/235141-235149/235123 (2012). https://doi.org:10.1103/PhysRevB.85.235149

6 Kresse, G. & Joubert, D. From ultrasoft pseudopotentials to the projector augmented-wave method. *Phys. Rev. B: Condens. Matter Mater. Phys.* **59**, 1758-1775 (1999).

7 Bloechl, P. E. Projector augmented-wave method. *Phys. Rev. B: Condens. Matter* **50**, 17953-17979 (1994).

8 Tang, W., Sanville, E. & Henkelman, G. A grid-based Bader analysis algorithm without lattice bias. *Journal of Physics: Condensed Matter* **21**, 084204 (2009). https://doi.org:10.1088/0953-8984/21/8/084204

9 Sanville, E., Kenny, S. D., Smith, R. & Henkelman, G. Improved grid-based algorithm for Bader charge allocation. *Journal of Computational Chemistry* **28**, 899-908 (2007). https://doi.org:https://doi.org/10.1002/jcc.20575

10 Henkelman, G., Arnaldsson, A. & Jónsson, H. A fast and robust algorithm for Bader decomposition of charge density. *Computational Materials Science* **36**, 354-360 (2006). https://doi.org:https://doi.org/10.1016/j.commatsci.2005.04.010

11 Vannice's entropy treatment utilizes an empirical equation based on the Sackur-Tetrode equation that requires treating the terms within the natural logarithm as unitless parameters. This more convenient treatment yields the same dependence on surface concentration as the more formal 2D Sackur-Tetrode equation derived by Campbell and coworkers in reference 37.

12 Campbell, C. T. & Sellers, J. R. V. The Entropies of Adsorbed Molecules. *Journal of the American Chemical Society* **134**, 18109-18115 (2012). https://doi.org:10.1021/ja3080117

13 Campbell, C. T., Sprowl, L. H. & Árnadóttir, L. Equilibrium Constants and Rate Constants for Adsorbates: Two-Dimensional (2D) Ideal Gas, 2D Ideal Lattice Gas, and Ideal Hindered Translator Models. *The Journal of Physical Chemistry C* **120**, 10283-10297 (2016). https://doi.org:10.1021/acs.jpcc.6b00975